INORGANIC CHEMISTRY FRONTIERS

RESEARCH ARTICLE

View Article Online
View Journal | View Issue

Cite this: *Inorg. Chem. Front.*, 2023, **10**, 3577

Successive redox modulation in an iron(II) spin-crossover framework†

Bang-Heng Lyu, Ze-Yu Ruan, Wen Cui, Si-Guo Wu, * Zhao-Ping Ni * and Ming-Liang Tong *

Received 7th April 2023,
Accepted 14th May 2023

DOI: 10.1039/d3qi00644a

rsc.li/frontiers-inorganic

Spin crossover (SCO) complexes capable of exhibiting distinct spin states under external stimuli have aroused intensive interest in materials science. Herein, we report an inverse-Hofmann-type metal–organic framework (MOF) $[Fe^{II}(TPPE)\{Au^{I}(CN)_2\}]I\cdot 2H_2O\cdot 7TCE$ (**1**, TPPE = 1,1,2,2-tetrakis(4-(pyridin-4-yl)phenyl)-ethene, TCE = 1,1,2,2-tetrachloroethane) with hysteretic SCO behavior. Most importantly, the redox-active unit $[Au^{I}(CN)_2]^-$ in **1** can be sequentially oxidized by I_2 and Br_2 to form the corresponding $[Au^{III}(CN)_2X_2]^-$ units *via* single-crystal to single-crystal transformation, and then reduced to $[Au^{I}(CN)_2]^-$ by L-ascorbic acid (AA). Accordingly, the SCO behavior is first regulated by successive redox reactions in the SCO field, which provides a platform for developing multi-responsive materials.

Introduction

Bistable materials with switchable physical properties have garnered continuous research interest due to their potential application in developing next-generation molecule-based sensors and actuators responding to external stimuli.[1–7] Notably, iron(II) spin crossover (SCO) materials are some of the most promising candidates for molecular switches as their spin states can be manipulated between paramagnetic high-spin (HS) and diamagnetic low-spin (LS) states under various external stimuli (such as temperature, irradiation, pressure and guest molecules).[8–11] Spin transition involving the rearrangement of the electronic configuration in the SCO-active center is accompanied by prominent structural transformations and changes in optical, magnetic, electronic and mechanical properties, which leads to their wide application in displays, chemical sensors and memory elements.[12–15]

SCO behaviors are closely related to the synergetic effect among spin centres.[16,17] Enormous efforts have been devoted to modulating the cooperativity so as to develop SCO materials with thermal hysteresis or stepwise SCO character. Recent studies suggest that the covalent ligation strategy where spin centers are bridged by organic/cyanometallate ligands can efficiently reinforce the cooperativity in SCO systems. One-dimensional (1D) $[Fe(Rtrz)_3]A_2\cdot nH_2O$ and 2D/3D Hofmann-type metal–organic frameworks (MOFs) can show fascinating SCO behaviors, and are regarded as archetype systems for theoretical research and nanodevice fabrication.[18–20] In addition, exploiting SCO materials with multi-responsive capability or successively switchable states is a burgeoning demand for designing multi-grade molecular switches and high-order magnetic storage. For example, taking advantage of host–guest interactions and opto-magnetic couplings, guest-programmable SCO behaviors and light-induced spin-state changes are implemented in SCO frameworks.[21–25] However, the influence of host–guest interactions mediated by intermolecular hydrogen bonding or aromatic stacking on the synergistic effect and the intrinsic multistability is unpredictable, which limits the modulation of the cooperativity.

Modifying the ligand field of the spin center *via* post-synthetic modification (PSM) is an advisable choice for modulating the synergetic effect. Recently, redox PSM onto cyanometallate/polyoxometalate linkers has been proven to be an effective method for controlling the spin transition temperature or regulating SCO behaviors.[26–29] Especially, hysteretic three- and two-stepped SCO behaviors were achieved by oxidative addition of different halogen molecules onto the open metal sites in the cationic framework of $[Fe^{II}(TPB)\{Au^{I}(CN)_2\}]^+$ (TPB = 1,2,4,5-tetra(pyridine-4-yl)benzene).[29] However, no successive redox PSM has been investigated for SCO materials until now.

Recently, a new inverse-Hofmann-type MOF $[Fe^{II}(TPPE)\{Au^{I}(CN)_2\}]ClO_4\cdot 14MeOH\cdot 18H_2O\cdot CH_2Cl_2$ (TPPE = 1,1,2,2-tetrakis(4-(pyridin-4-yl)phenyl)-ethene) was reported, which exhibits abrupt and incomplete SCO behavior and synergistic SCO-

Key Laboratory of Bioinorganic and Synthetic Chemistry of Ministry of Education, School of Chemistry, Sun Yat-Sen University, Guangzhou, 510275, P. R. China. E-mail: wusg6@mail.sysu.edu.cn, nizhp@mail.sysu.edu.cn, tongml@mail.sysu.edu.cn

†Electronic supplementary information (ESI) available: Crystallographic data and additional IR, XPS, and magnetic figures. CCDC 2249182 (**1**-120 K), 2249183 (**1**-300 K), 2249190 (**2**-102 K), 2249191 (**2**-320 K) and 2249194 (**3**-120 K). For ESI and crystallographic data in CIF or other electronic format see DOI: https://doi.org/10.1039/d3qi00644a

fluorescence property.[30] Taking advantage of the large guest-accessible channels and open metal sites of Au^I, herein, we report a modified compound $[Fe^{II}(TPPE)\{Au^I(CN)_2\}]I{\cdot}2H_2O{\cdot}7TCE$ (**1**, TCE = 1,1,2,2-tetrachloroethane) with high boiling point solvents, which shows a hysteretic SCO behavior. Air-stable crystal samples with good crystallinity were successfully obtained, which provide a good platform to explore successive redox PSM *via* single-crystal to single-crystal transformation. It can be sequentially oxidized by I_2 and Br_2 to form $[Fe^{II}(TPPE)\{Au^{III}(CN)_2I_2\}]I_3{\cdot}7TCE$ (**2**) and $[Fe^{II}(TPPE)\{Au^{III}(CN)_2Br_2\}]Br_3{\cdot}H_2O{\cdot}8TCE$ (**3**) and then reduced by L-ascorbic acid (AA) to form $[Fe^{II}(TPPE)\{Au^I(CN)_2\}]Br{\cdot}3H_2O{\cdot}8TCE$ (**4**). Hence, the hysteretic SCO behavior has been regulated by a successive redox PSM process for the first time.

Experimental

Materials and methods

All the reagents and solvents were commercially available and used without further purification. Elemental analyses of C, H and N were carried out using an Elementar Vario-EL CHNS elemental analyzer. Thermogravimetric analyses (TGA) were performed on a TA Instruments NETZSCH TG 209 F3 under a nitrogen flow atmosphere at a heating rate of 10 K min^{-1}. FT-IR spectra were measured on a Bruker Vertex70 Hyperion 3000 instrument in crystal samples. Raman spectra were collected using a Renishaw inVia Qontor instrument equipped with a 785 nm laser source. X-ray photoelectron spectroscopy (XPS) measurements were performed on a Thermo Fisher Scientific ESCALAB Xi+ system using an Al-K_α source. Variable temperature magnetic susceptibilities of polycrystalline samples were measured on a Quantum Design PPMS3 SQUID magnetometer under an applied field of 5 kOe with a sweeping rate of 2 K min^{-1}. The diamagnetic contribution was calculated based on Pascal's constants. Powder X-ray diffraction (PXRD) patterns were obtained on a Rigaku SmartLab X-ray diffractometer (Cu-K_α, λ = 1.54056 Å) in the capillary test mode at room temperature.

Synthetic procedures

$[Fe^{II}(TPPE)\{Au^I(CN)_2\}]I{\cdot}2H_2O{\cdot}7TCE$ (1). $K[Au^I(CN)_2]{\cdot}2H_2O$ (0.025 mmol) and TPPE (0.025 mmol) were dissolved in 4.5 mL of TCE/MeOH solution (v : v = 2 : 1) and placed in the bottom of a test tube. Then, 9 mL of TCE/MeOH solution (v : v = 1 : 1) was carefully added as the buffer solution, followed by 2.5 mL of methanol solution of FeI_2 (0.025 mmol) at the top. Yellow block crystals suitable for single crystal X-ray measurement were obtained after 2 weeks. Yield: 89.3%. Anal. calcd for $C_{62}H_{50}N_6FeIAuO_2Cl_{28}$: C, 32.61; H, 2.21; N, 3.68. Found: C, 32.33; H, 2.15; N, 3.96.

$[Fe^{II}(TPPE)\{Au^{III}(CN)_2I_2\}]I_3{\cdot}7TCE$ (2). Yellow crystals of complex **1** were soaked in 4 mL of 0.1 M I_2 solution (TCE : MeOH = 1 : 1) for 30 min, and then black crystals suitable for single crystal X-ray measurement were obtained. Yield: 60.1%. Anal. calcd for $C_{62}H_{46}N_6FeI_5AuCl_{28}$: C, 27.03; H, 1.68; N, 3.05. Found: C, 27.14; H, 1.66; N, 3.35.

$[Fe^{II}(TPPE)\{Au^{III}(CN)_2Br_2\}]Br_3{\cdot}H_2O{\cdot}8TCE$ (3). Black crystals of complex **2** were soaked in 4 mL of 0.05 M Br_2 and 1 M PPh_4Br solution (TCE : MeOH = 1 : 1) for 15 min, and then brown red crystals suitable for single crystal X-ray measurement were obtained. Yield: 49.6%. Anal. calcd for $C_{64}H_{50}N_6FeBr_5AuOCl_{32}$: C, 28.41; H, 1.86; N, 3.11. Found: C, 28.29; H, 1.80; N, 3.37.

$[Fe^{II}(TPPE)\{Au^I(CN)_2\}]Br{\cdot}3H_2O{\cdot}8TCE$ (4). Brown red complex **3** was immersed in 10 mL of 0.05 M AA solution (TCE : MeOH = 1 : 1) overnight until the sample color changed to yellow. The powder sample was washed three times with the mixed solution (TCE : MeOH = 1 : 1) and then filtered. Yield: 24.8%. Anal. calcd for $C_{64}H_{54}N_6FeBrAuO_3Cl_{32}$: C, 31.73; H, 2.25; N, 3.47. Found: C, 31.36; H, 2.10; N, 3.83.

X-ray crystallography

Variable temperature single crystal X-ray diffraction data of complexes **1–3** were collected on a Bruker D8 QUEST diffractometer with Mo-K_α radiation (λ = 0.71073 Å). The structures were solved using intrinsic phasing methods and all non-hydrogen atoms were refined with anisotropic displacement parameters by least-squares on F^2 values using the SHELXL program in OLEX2.[31–33] The hydrogen atoms were refined using a riding model. The solvents in the lattice of **1–3** are highly disordered and were omitted using a solvent mask. The single crystal of **3** was partly degraded during the oxidation process and only the low-temperature structure was measured. Crystallographic data for this paper can be obtained from the Cambridge Crystallographic Data Centre (CCDC) with deposition numbers 2249182 (**1**-120 K), 2249183 (**1**-300 K), 2249190 (**2**-102 K), 2249191 (**2**-320 K) and 2249194 (**3**-120 K).†

Results and discussion

Crystal structures

Complex **1** was synthesized *via* slow diffusion of $K[Au^I(CN)_2]$ and TPPE into FeI_2 in TCE/MeOH solution. After soaking **1** in 0.1 M I_2 for 30 min, **2** was isolated as the oxidative addition product with the color changing from yellow to black. When **2** further reacted with 0.05 M Br_2 for 15 min, brown red **3** was isolated as the halogen-substituted product. When **3** was treated with 0.05 M AA, pale yellow **4** was obtained as the reduction product (Fig. 1).

Single-crystal X-ray diffraction (SC-XRD) experiments indicate that **1** crystallizes in the orthorhombic *Pmmm* space group at 120 and 300 K (Table S1, ESI†), which is different from the reported $[Fe(TPPE)\{Au(CN)_2\}]ClO_4{\cdot}14MeOH{\cdot}18H_2O{\cdot}CH_2Cl_2$ in the space group *Pbam* at 173 K.[30] As shown in Fig. 2, each Fe^{II} center is equatorially coordinated by four tetradentate TPPE ligands within the *bc* plane and is axially bridged by two $[Au^I(CN)_2]^-$ pillars along the *a* axis, giving rise to a 3D inverse-Hofmann-type framework.[34] The pyridyl and phenyl groups of TPPE ligands are twofold disordered at 120 and 300 K. Since

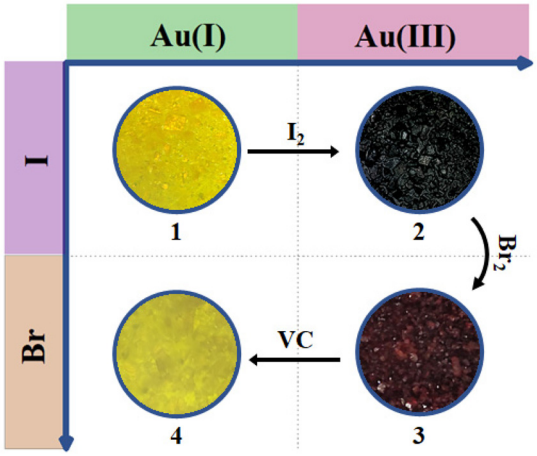

Fig. 1 Chemical-redox procedures and relative color changes recorded at room temperature.

the TPPE ligand is longer than the TPB ligand, the I^- ions are far away from the Au^I ions, which is different from the presence of weak I···Au interactions in $[Fe(TPB)Au(CN)_2]I{\cdot}4H_2O{\cdot}4DMF$.[29] Water and tetrachloroethane molecules are highly disordered in the lattice and were squeezed *via* a solvent mask operation in Olex2. The guest composition was determined by elemental analysis and thermogravimetric analysis. The average Fe–N bond length is 1.970 Å at 120 K and 2.198 Å at 300 K, revealing an SCO behavior of Fe^{II} from LS to HS states (Table S4, ESI†). Amid spin transition, the unit cell volume increases by 8.6%.

Complex **2** was obtained *via* single-crystal to single-crystal transformation from **1** after redox-PSM by I_2 solution. SC-XRD reveals that **2** crystallizes in the *Pmmm* space group at 320 K, but in the *Fmmm* space group with an 8-fold unit cell volume at 102 K (Table S2, ESI†). It should be due to the fact that the disordered TPPE ligand becomes ordered at a low temperature.

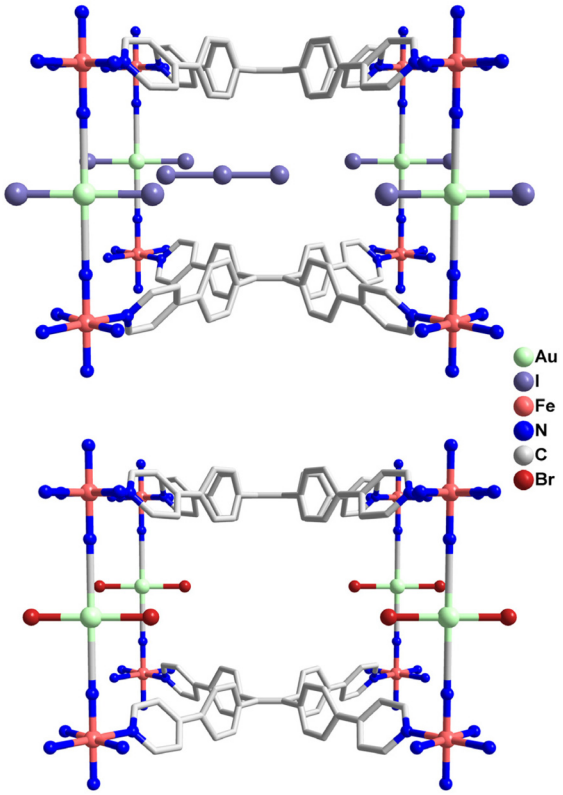

Fig. 3 Selected clathrate structures of **2** (102 K, up) and **3** (120 K, down).

As depicted in Fig. 3, **2** exhibits a similar skeleton to **1** except that the linear $[Au^I(CN)_2]^-$ linkers are transferred to square planar *trans*-$[Au^{III}(CN)_2I_2]^-$ units after the oxidative addition of I_2 onto the Au^I site. The coordinated I atoms are disordered around Au^{III} with an Au^{III}–I length of about 2.61 Å. Meanwhile, the I^- anions complex with I_2 to generate I_3^- anions, which lie

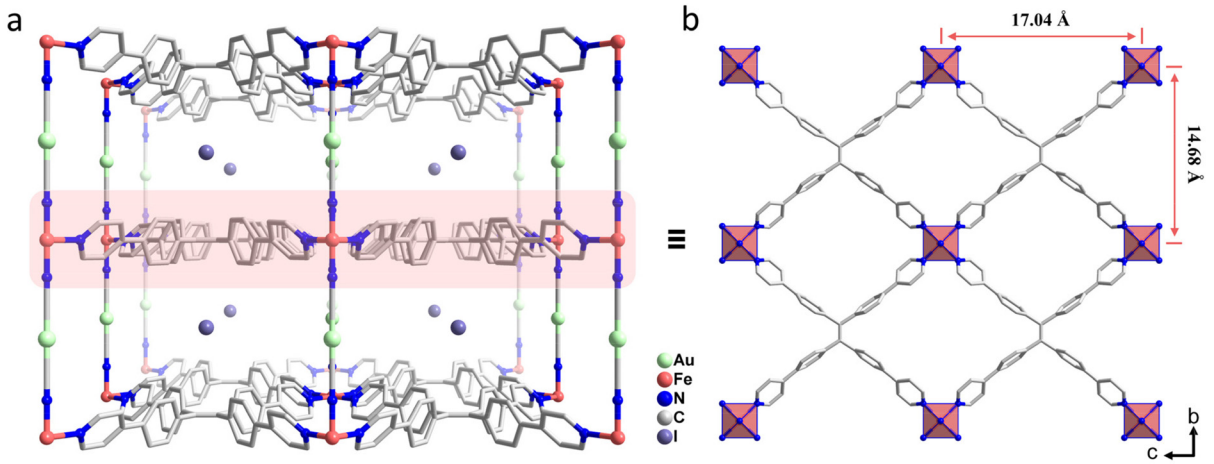

Fig. 2 (a) Perspective view of **1** (120 K) along the *c* axis, (b) the 2D network of $[Fe(TPPE)]_n$ extends in the (100) plane. The hydrogen atoms and guest molecules are omitted for clarity.

between the neighbouring $[Fe(TPPE)]_n$ layers. The average Fe–N distances of 1.962 Å at 102 K and 2.199 Å at 320 K are consistent with the LS and HS states of Fe^{II} ions in the octahedral $[FeN_6]$ environment. Meanwhile, the octahedral distortion parameter $\sum$Fe in **2** decreases from 14.5° to 3.58°, which is different from the small variation in **1** (Tables S4 and S5, ESI†).

Successive single-crystal to single-crystal transformation was achieved by immersing **2** in Br_2 solution which yields the bromide oxidative addition product **3**. Since the crystal quality is partially damaged during the structural transformation, only the low-temperature structure of **3** was solved with modest refinement. As depicted in Fig. 3, the 3D framework is similar except that the *trans*-$[Au^{III}(CN)_2I_2]^-$ unit in **2** is replaced by the *trans*-$[Au^{III}(CN)_2Br_2]^-$ linker in **3**. The Br_3^- anion serves as the counter anion, which is confirmed by elemental analysis and Raman spectroscopy (*vide infra*). The bond lengths of Au^{III}–Br and Au^{III}–C are 2.40 and 1.96 Å at 120 K, respectively, within the reasonable range reported in the literature (Table S6, ESI†).[35,36] The $\langle Fe–N\rangle_{av}$ distance is 1.990 Å for **3** at 120 K, corresponding to the LS state.

As evidenced by powder X-ray diffraction (PXRD) patterns (Fig. S5–S8, ESI†), the frameworks of **1–4** remain robust during the redox PSM process. The PXRD patterns for **1** and **2** are well comparable with their simulated ones. The slight shifts of the experimental PXRD pattern of **3** should be due to spin transition (*vide infra*) at different measuring temperatures. Notably, the PXRD pattern of the reduction product **4** is in good agreement with the simulated pattern of the initial complex **1**, indicating a reversible redox modulation.

Raman/IR/XPS spectra

Stepwise redox transformations were further confirmed by Raman and infrared spectroscopy at room temperature (Fig. 4). When **1** was oxidized to **2** by I_2, two new strong Raman peaks appeared at 112 and 142 cm^{-1}, which can be assigned to the stretching vibrations of the I_3^- anion and the Au^{III}–I bond, respectively.[37,38] When **2** was further oxidized to **3** by Br_2, the strongest υ_{Au-I} peak in **2** disappeared and two modest peaks at 169 and 206 cm^{-1} corresponding to the characteristic vibrations of the Br_3^- anion and the Au^{III}–Br bond appeared in **3**.[37,39,40] After treatment with AA, these characteristic peaks

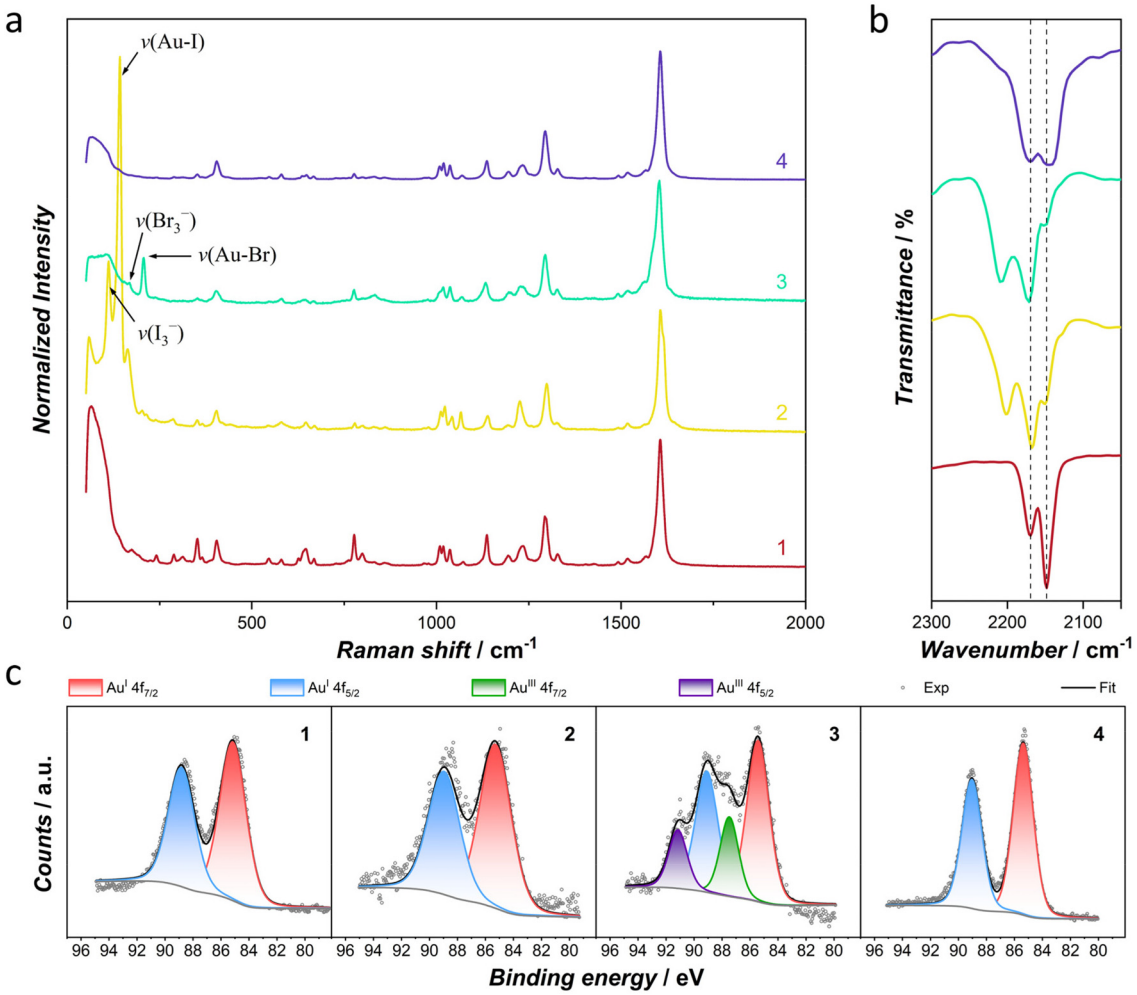

Fig. 4 Selected Raman (a), infrared spectra (b) and X-ray photoelectron spectroscopy of Au 4f (c) for chemo-redox processes.

smeared out in **4**, indicating the complete reduction of Au^{III} and the trihalide anions.

Infrared spectra reveal the changes in the vibration of the cyanide group ($\upsilon_{C\equiv N}$) during redox processes. For **1**, the $\upsilon_{C\equiv N}$ signals are observed at 2148 and 2169 cm^{-1}, common for the dicyanoaurate(I) modules in SCO-MOFs.[29,37] After oxidation from **1** to **2**, the σ-bonding between cyanide and Au^{III} in the $[Au^{III}(CN)_2I_2]^-$ unit is strengthened, which leads to a blue shift of $\upsilon_{C\equiv N}$ signals to 2167 and 2202 cm^{-1}, respectively. Similarly, the $\upsilon_{C\equiv N}$ signals in **3** are observed at 2171 and 2208 cm^{-1}. Moreover, we noticed that the signal at 2148 cm^{-1} becomes a shoulder peak, which still exists in **2** and **3**. Hence, complex **1** was tested to react with I_2 for a longer time. However, the signal at 2148 cm^{-1} still exists in the oxidation product after 120 min reaction time (Fig. S13, ESI†). Additionally, the framework starts to decompose with a longer reaction time or a higher concentration of the oxidant. Therefore, this shoulder peak in **2** and **3** may be due to a trace amount of the unoxidized substance and/or asymmetric perturbation of the cyanide groups by the Au ions induced by disordered halogen atoms.[41,42] When **3** was reduced by AA, the $\upsilon_{C\equiv N}$ peaks of **4** come back to 2144 and 2169 cm^{-1}, verifying the successful reduction of Au^{III} to the initial oxidative state.

X-ray photoelectron spectroscopy was performed to monitor the change of oxidation states of Au. For **1**, the doublet recorded with binding energies of 85.20 and 88.85 eV is characteristic of the Au^I 4f peaks with spin–orbit splitting.[43] For the oxidative addition product **2**, only $4f_{7/2}$ and $4f_{5/2}$ signals for Au^I were recorded, which is due to the radiation-induced damage on Au^{III} and it results in the reduction of the metal ion by electron beams.[44,45] In **3**, two new peaks were observed with higher binding energies of 87.50 and 91.15 eV, which is strong evidence for Au^{III} 4f doublets. The distinct photoreduction efficiency of **2** and **3** might be related to stronger linkage of the Au–Br bond. Fitting the Au 4f signal with the restricted intervals and area ratios of two doublets gives rise to Au^{III} components of 29% in **3**. Complex **4** displays only the Au^I 4f doublet at 85.40 and 89.05 eV, respectively, verifying the reversible redox modulation.

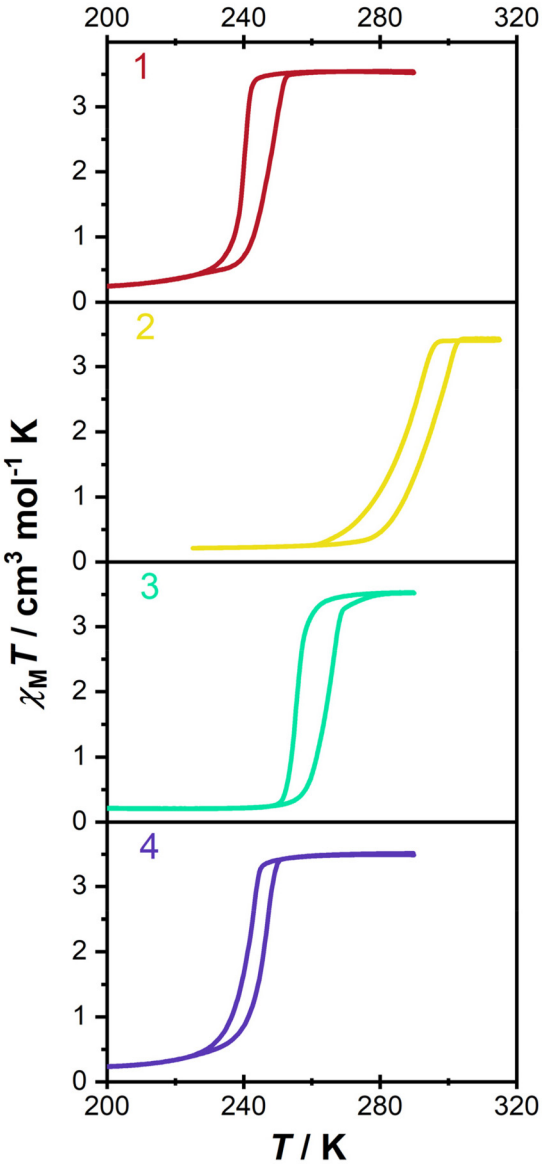

Fig. 5 Variable-temperature molar magnetic susceptibility corresponding to the chemo-redox processes.

Magnetic properties

To investigate the redox-modulated SCO behaviors, magnetic susceptibility measurements were performed with a sweeping rate of 2 K min^{-1}. As shown in Fig. 5, the χT values in **1** are around 0.3/3.5 cm^3 mol^{-1} K at low/high-temperature regions, revealing the LS/HS states of Fe^{II}. Compared with the incomplete SCO behavior in $[Fe^{II}(TPPE)\{Au^I(CN)_2\}]ClO_4{\cdot}14MeOH{\cdot}18H_2O{\cdot}CH_2Cl_2$,[30] complex **1** displays a complete and hysteretic SCO behavior with critical temperatures of 240 K in the cooling process ($T_{c\downarrow}$) and 247 K in the warming process ($T_{c\uparrow}$), giving rise to a hysteresis loop (ΔT) of 7 K. These distinctions might be caused by the changes of anions and solvent molecules, which result in disparate host–guest interactions across the lattice.

When **1** was oxidized by I_2, hysteretic SCO behavior was still observed in **2**. However, the T_c values shifted toward the higher temperature region and approached 288/295 K in cooling/warming modes. In contrast, the T_c values of **3** moved back to 256/265 K and then the hysteresis loop widened to 9 K. Hence, the oxidative addition product of Br_2 exhibits a lower T_c than that of I_2, which is analogous to the trend in the [Fe(pyrazine){$Pt(CN)_4X$}] system.[26] The weaker ligand field in the bromide-additive species is due to the weakening of the σ-bonding between cyanide and Au^{III} with the increased electronegativity of halogen. After reduction treatment with AA, the SCO behavior in **4** returns to the initial spin transition region ($T_{c\downarrow}$ = 241 K, $T_{c\uparrow}$ = 246 K) with a shrunken ΔT value of 5 K. A slight deviation of SCO behavior between **1** and **4** may be caused by anions and/or the downscale effect.[46,47] SCO behaviors for **1–4** were further confirmed by multiple thermal cycles of magnetic data (Fig. S18–S21, ESI†), which illustrates

the reliability of redox regulation and their potential application in developing multi-responsive materials.

Conclusions

By employing a high boiling point solvent, we reported a modified inverse-Hofmann-type Fe^{II} SCO framework with good crystallinity and stability. The porous structure of the framework enables the open metal sites of Au^{I} to undergo oxidative addition with I_2 and Br_2. Most importantly, such redox PSM can be manipulated step by step by making good use of the oxidation order of halogens. The Au^{III} species in the skeleton can be reversibly reduced to Au^{I} by AA. Although they still show hysteretic SCO behaviors, the spin transition temperature is significantly modulated by the redox PSM. The results reported in this work demonstrate for the first time that successive redox modulation can be realized in SCO materials.

Conflicts of interest

There are no conflicts to declare.

Acknowledgements

This work was supported by the National Key Research and Development Program of China (2018YFA0306001), the NSFC (grant no. 22271322 and 21773316), the Pearl River Talent Plan of Guangdong (2017BT01C161) and the Guangdong Special Fund for Science and Technology Innovation Strategy (pdjh2023b0019).

Notes and references

1 J. A. Rodríguez-Velamazán, M. A. González, J. A. Real, M. Castro, M. C. Muñoz, A. B. Gaspar, R. Ohtani, M. Ohba, K. Yoneda, Y. Hijikata, N. Yanai, M. Mizuno, H. Ando and S. Kitagawa, A switchable molecular rotator: neutron spectroscopy study on a polymeric spin-crossover compound, *J. Am. Chem. Soc.*, 2012, **134**, 5083–5089.

2 D. Aguila, Y. Prado, E. S. Koumousi, C. Mathoniere and R. Clerac, Switchable Fe/Co Prussian blue networks and molecular analogues, *Chem. Soc. Rev.*, 2016, **45**, 203–224.

3 M. D. Manrique-Juárez, S. Rat, L. Salmon, G. Molnár, C. M. Quintero, L. Nicu, H. J. Shepherd and A. Bousseksou, Switchable molecule-based materials for micro- and nanoscale actuating applications: Achievements and prospects, *Coord. Chem. Rev.*, 2016, **308**, 395–408.

4 O. Sato, Dynamic molecular crystals with switchable physical properties, *Nat. Chem.*, 2016, **8**, 644–656.

5 Y. S. Meng and T. Liu, Manipulating spin transition to achieve switchable multifunctions, *Acc. Chem. Res.*, 2019, **52**, 1369–1379.

6 Z. S. Yao, Z. Tang and J. Tao, Bistable molecular materials with dynamic structures, *Chem. Commun.*, 2020, **56**, 2071–2086.

7 W. Huang, X. Ma, O. Sato and D. Wu, Controlling dynamic magnetic properties of coordination clusters *via* switchable electronic configuration, *Chem. Soc. Rev.*, 2021, **50**, 6832–6870.

8 Z.-P. Ni, J.-L. Liu, M. N. Hoque, W. Liu, J.-Y. Li, Y.-C. Chen and M.-L. Tong, Recent advances in guest effects on spin-crossover behavior in Hofmann-type metal-organic frameworks, *Coord. Chem. Rev.*, 2017, **335**, 28–43.

9 P. Gütlich, Y. Garcia and H. A. Goodwin, Spin crossover phenomena in Fe(II) complexes, *Chem. Soc. Rev.*, 2000, **29**, 419–427.

10 M. C. Muñoz and J. A. Real, Thermo-, piezo-, photo- and chemo-switchable spin crossover iron(II)-metallocyanate based coordination polymers, *Coord. Chem. Rev.*, 2011, **255**, 2068–2093.

11 K. Senthil Kumar and M. Ruben, Emerging trends in spin crossover (SCO) based functional materials and devices, *Coord. Chem. Rev.*, 2017, **346**, 176–205.

12 M. Ohba, K. Yoneda, G. Agustí, M. C. Muñoz, A. B. Gaspar, J. A. Real, M. Yamasaki, H. Ando, Y. Nakao, S. Sakaki and S. Kitagawa, Bidirectional chemo-switching of spin state in a microporous framework, *Angew. Chem., Int. Ed.*, 2009, **48**, 4767–4771.

13 L. Zhao, Y.-S. Meng, Q. Liu, O. Sato, Q. Shi, H. Oshio and T. Liu, Switching the magnetic hysteresis of an [Fe^{II}–NC–W^{V}]-based coordination polymer by photoinduced reversible spin crossover, *Nat. Chem.*, 2021, **13**, 698–704.

14 R. Torres-Cavanillas, M. Morant-Giner, G. Escorcia-Ariza, J. Dugay, J. Canet-Ferrer, S. Tatay, S. Cardona-Serra, M. Giménez-Marqués, M. Galbiati, A. Forment-Aliaga and E. Coronado, Spin-crossover nanoparticles anchored on MoS_2 layers for heterostructures with tunable strain driven by thermal or light-induced spin switching, *Nat. Chem.*, 2021, **13**, 1101–1109.

15 S. Liu, K. Zhou, T. Yuan, W. Lei, H.-Y. Chen, X. Wang and W. Wang, Imaging the thermal hysteresis of single spin-crossover nanoparticles, *J. Am. Chem. Soc.*, 2020, **142**, 15852–15859.

16 J. Cruddas and B. J. Powell, Spin-state ice in elastically frustrated spin-crossover materials, *J. Am. Chem. Soc.*, 2019, **141**, 19790–19799.

17 M. Paez-Espejo, M. Sy and K. Boukheddaden, Elastic frustration causing two-step and multistep transitions in spin-crossover solids: emergence of complex antiferroelastic structures, *J. Am. Chem. Soc.*, 2016, **138**, 3202–3210.

18 O. Kahn and C. J. Martinez, Spin-transition polymers: from molecular materials toward memory devices, *Science*, 1998, **279**, 44–48.

19 T. Kitazawa, Y. Gomi, M. Takahashi, M. Takeda, M. Enomoto, A. Miyazaki and T. Enoki, Spin-crossover behaviour of the coordination polymer $Fe^{II}(C_5H_5N)_2Ni^{II}(CN)_4$, *J. Mater. Chem.*, 1996, **6**, 119–121.

20 V. Niel, J. M. Martinez-Agudo, M. C. Muñoz, A. B. Gaspar and J. A. Real, Cooperative spin crossover behavior in cyanide-bridged Fe(II)–M(II) bimetallic 3D Hofmann-like networks (M = Ni, Pd, and Pt), *Inorg. Chem.*, 2001, **40**, 3838–3839.

21 M. J. Murphy, K. A. Zenere, F. Ragon, P. D. Southon, C. J. Kepert and S. M. Neville, Guest programmable multistep spin crossover in a porous 2-D Hofmann-type material, *J. Am. Chem. Soc.*, 2017, **139**, 1330–1335.

22 W. Liu, Y.-Y. Peng, S.-G. Wu, Y.-C. Chen, M. N. Hoque, Z.-P. Ni, X.-M. Chen and M.-L. Tong, Guest-switchable multistep spin transitions in an amine-functionalized metal–organic framework, *Angew. Chem., Int. Ed.*, 2017, **56**, 14982–14986.

23 X. Bao, H. J. Shepherd, L. Salmon, G. Molnár, M.-L. Tong and A. Bousseksou, The effect of an active guest on the spin crossover phenomenon, *Angew. Chem., Int. Ed.*, 2013, **52**, 1198–1202.

24 E. Milin, V. Patinec, S. Triki, E.-E. Bendeif, S. Pillet, M. Marchivie, G. Chastanet and K. Boukheddaden, Elastic frustration triggering photoinduced hidden hysteresis and multistability in a two-dimensional photoswitchable Hofmann-like spin-crossover metal–organic framework, *Inorg. Chem.*, 2016, **55**, 11652–11661.

25 Y.-C. Chen, Y. Meng, Y.-J. Dong, X.-W. Song, G.-Z. Huang, C.-L. Zhang, Z.-P. Ni, J. Navařík, O. Malina, R. Zbořil and M.-L. Tong, Light- and temperature-assisted spin state annealing: accessing the hidden multistability, *Chem. Sci.*, 2020, **11**, 3281–3289.

26 G. Agusti, R. Ohtani, K. Yoneda, A. B. Gaspar, M. Ohba, J. F. Sanchez-Royo, M. C. Munoz, S. Kitagawa and J. A. Real, Oxidative addition of halogens on open metal sites in a microporous spin-crossover coordination polymer, *Angew. Chem., Int. Ed.*, 2009, **48**, 8944–8947.

27 R. Ohtani, K. Yoneda, S. Furukawa, N. Horike, S. Kitagawa, A. B. Gaspar, M. C. Muñoz, J. A. Real and M. Ohba, Precise Control and Consecutive Modulation of spin transition temperature using chemical migration in porous coordination polymers, *J. Am. Chem. Soc.*, 2011, **133**, 8600–8605.

28 M. Palacios-Corella, V. García-López, J. C. Waerenborgh, B. J. C. Vieira, G. Mínguez Espallargas, M. Clemente-León and E. Coronado, Redox and guest tunable spin-crossover properties in a polymeric polyoxometalate, *Chem. Sci.*, 2023, **14**, 3048–3055.

29 S. G. Wu, L. F. Wang, Z. Y. Ruan, S. N. Du, S. Gomez-Coca, Z. P. Ni, E. Ruiz, X. M. Chen and M. L. Tong, Redox-programmable spin-crossover behaviors in a cationic framework, *J. Am. Chem. Soc.*, 2022, **144**, 14888–14896.

30 X.-R. Wu, Z.-K. Liu, M. Zeng, M.-X. Chen, J. Tao, S.-Q. Wu and H.-Z. Kou, Fluorescence emission modulation in cyanido-bridged Fe(II) spin crossover coordination polymers, *Sci. China: Chem.*, 2022, **65**, 1569–1576.

31 G. M. Sheldrick, SHELXT – Integrated space-group and crystal-structure determination, *Acta Crystallogr., Sect. A: Found. Adv.*, 2015, **71**, 3–8.

32 G. M. Sheldrick, A short history of SHELX, *Acta Crystallogr., Sect. A: Found. Crystallogr.*, 2008, **64**, 112–122.

33 O. V. Dolomanov, L. J. Bourhis, R. J. Gildea, J. A. K. Howard and H. Puschmann, OLEX2: a complete structure solution, refinement and analysis program, *J. Appl. Crystallogr.*, 2009, **42**, 339–341.

34 J. H. Yang, Y. X. Zhao, J. P. Xue, Z. S. Yao and J. Tao, Reverse Hofmann-Type Spin-crossover compound showing a multichannel controllable color change in an ambient environment, *Inorg. Chem.*, 2021, **60**, 7337–7344.

35 J. S. Ovens, K. N. Truong and D. B. Leznoff, Structural organization and dimensionality at the hands of weak intermolecular Au···Au, Au···X and X···X (X = Cl, Br, I) interactions, *Dalton Trans.*, 2012, **41**, 1345–1351.

36 J. S. Ovens, K. N. Truong and D. B. Leznoff, Targeting $[AuCl_2(CN)_2]^-$ units as halophilic building blocks in coordination polymers, *Inorg. Chim. Acta*, 2013, **403**, 127–135.

37 K. Nakamoto, *Infrared and Raman spectra of inorganic and coordination compounds*, John Wiley & Sons, Inc., Hoboken, New Jersey, 2009.

38 P. H. Svensson and L. Kloo, Synthesis, Structure, and bonding in polyiodide and metal iodide–iodine systems, *Chem. Rev.*, 2003, **103**, 1649–1684.

39 X. Chen, M. A. Rickard, J. W. Hull, Jr., C. Zheng, A. Leugers and P. Simoncic, Raman spectroscopic investigation of tetraethylammonium polybromides, *Inorg. Chem.*, 2010, **49**, 8684–8689.

40 J. S. Ovens and D. B. Leznoff, Thermal expansion behavior of $M^I[AuX_2(CN)_2]$-based coordination polymers (M = Ag, Cu; X = CN, Cl, Br), *Inorg. Chem.*, 2017, **56**, 7332–7343.

41 J. S. Ovens, A. R. Geisheimer, A. A. Bokov, Z.-G. Ye and D. B. Leznoff, The use of polarizable $[AuX_2(CN)_2]^-$ (X = Br, I) building blocks toward the formation of birefringent coordination polymers, *Inorg. Chem.*, 2010, **49**, 9609–9616.

42 J. S. Ovens and D. B. Leznoff, Raman detected sensing of volatile organic compounds by vapochromic Cu $[AuX_2(CN)_2]_2$ (X = Cl, Br) coordination polymer materials, *Chem. Mater.*, 2015, **27**, 1465–1478.

43 J. Moulder, W. Stickle, P. Sobol, K. Bomben and G. J. I. W. Muilenberg, *Handbook of X-ray photoelectron spectroscopy*, PerkinElmer, MA, USA, 1992.

44 P. Burroughs, A. Hamnett, J. F. McGilp and A. F. Orchard, Radiation damage in some platinum(IV) complexes produced during soft X-ray photoelectron spectroscopic studies, *J. Chem. Soc., Faraday Trans. 2*, 1975, **71**, 177–187.

45 F. Karadas, G. Ertas, E. Ozkaraoglu and S. Suzer, X-ray-induced production of gold nanoparticles on a SiO_2/Si system and in a poly(methyl methacrylate) matrix, *Langmuir*, 2005, **21**, 437–442.

46 I. Boldog, A. B. Gaspar, V. Martínez, P. Pardo-Ibañez, V. Ksenofontov, A. Bhattacharjee, P. Gütlich and J. A. Real, Spin-crossover nanocrystals with magnetic, optical, and structural bistability near room temperature, *Angew. Chem., Int. Ed.*, 2008, **47**, 6433–6437.

47 F. Volatron, L. Catala, E. Rivière, A. Gloter, O. Stéphan and T. Mallah, Spin-crossover coordination nanoparticles, *Inorg. Chem.*, 2008, **47**, 6584–6586.